



HAL
open science

Characterization and modelling of a carbon ramming mix used in high-temperature industry

Jérôme Brulin, Amna Rekik, Laurent Josserand, Eric Blond, Alain Gasser, Frédéric
Roulet

► **To cite this version:**

Jérôme Brulin, Amna Rekik, Laurent Josserand, Eric Blond, Alain Gasser, et al.. Characterization and modelling of a carbon ramming mix used in high-temperature industry. *International Journal of Solids and Structures*, 2011, 48 (1), pp.854-864. <10.1016/j.ijsolstr.2010.11.024>. <hal-00652709>

HAL Id: hal-00652709

<https://hal.science/hal-00652709v1>

Submitted on 16 Dec 2011

HAL is a multi-disciplinary open access archive for the deposit and dissemination of scientific research documents, whether they are published or not. The documents may come from teaching and research institutions in France or abroad, or from public or private research centers.

L'archive ouverte pluridisciplinaire **HAL**, est destinée au dépôt et à la diffusion de documents scientifiques de niveau recherche, publiés ou non, émanant des établissements d'enseignement et de recherche français ou étrangers, des laboratoires publics ou privés.



HAL Authorization

1 Characterization and modelling of a carbon ramming
2 mix used in high-temperature industry

3 J. Brulin^{a,b}, A. Rekik^{a,*}, L. Josserand^a, E. Blond^a, A. Gasser^a, F. Roulet^b

4 ^a*Institut PRISME (EA 4229, University of Orléans), Polytech'Orléans*
5 *8, rue Léonard de Vinci, 45072 Orléans, France*

6 ^b*Saint-Gobain CREE, 550, avenue Alphonse Jauffret, BP 224, 84306 Cavaillon, France*

7 **Abstract**

This paper is devoted to the modelling of a specific ramming mix mainly used in the high-temperature industry due to its high-compacting behaviour. This material has the ability to absorb the deformation of parts submitted to high thermal loads. Triaxial and instrumented die compaction tests were carried out in order to identify the shear and hardening behaviours, respectively. Tests on the ramming mix were lead for a temperature range between 20°C and 80°C. The temperature effect is particularly observed on the material response when it is compacted. The main features of the behaviour of the ramming mix can be represented by the theoretical framework of the Modified Cam-Clay model. A single variable allows to accurately reproduce the hardening behaviour depending on the temperature. Moreover, an extension of the model for the hardening behaviour at high pressures is proposed. A good agreement between the experimental data and numerical tests is reached with this model.

8 *Keywords:* ramming mix, parameters identification, die compaction test,
9 triaxial test, temperature effect, FE method, Modified Cam-Clay model

*Principal corresponding author. Tel.: +33(0)2.38.47.24.33; Fax: +33(0)2.38.41.73.29
Email address: amna.rekik@univ-orleans.fr (A. Rekik)

10 **1. Introduction**

11 The steel industry requires huge structures mainly composed of refractory
12 materials. The thermomechanical properties of these materials suit perfectly
13 high temperature applications. However, the expansion of these constituents
14 can damage some parts of the structure. To avoid this damage, ramming
15 mixes are often used to absorb the deformations. Indeed, these loose ma-
16 terials are well-known for their high-compacting behaviour. An appropriate
17 modelling of this material must at least be able to reproduce the compaction
18 behaviour sensitive to the temperature effect.

19 This paper investigates the case of a ramming mix composed of graphite
20 (80%) and coal tar (20%). Its aspect can be compared with a bituminous
21 sand. In the literature, many studies were carried out in order to predict
22 the behaviour of loose geological materials (Bousshine et al., 2001; Liu and
23 Carter, 2002), pharmaceutical powders (Wu et al., 2005; Han et al., 2008) or
24 metallic powders (Park et al., 1999; Chtourou et al., 2002). The modelling
25 of loose materials whose behaviour is highly dependent on the porosity rate
26 is classically based on micro-mechanical and macro-mechanical approaches.
27 The first one assumes that each particle is a sphere. It takes also into account
28 the contact interactions between the particles (Helle et al., 1985; Fleck et al.,
29 1992; Biba et al., 1993; Fleck, 1995). From a discrete approach, the macro-
30 scopic behaviour of a material can be evaluated by means of homogeniza-
31 tion methods (Piat et al., 2004; Le et al., 2008). Although micro-mechanical
32 models are devoted to understand the physical behaviour of the constituents,
33 macro-mechanical models (Shima and Oyane, 1976; Gurson, 1977; Haggblad,
34 1991) are well-adapted for engineering applications which often occur at a
35 large scale. The phenomenological models were mainly developed for applica-
36 tions in soil mechanics, such as the Drucker-Prager Cap model (Drucker and
37 Prager, 1952), the Modified Cam-Clay model (Roscoe and Burland, 1968)
38 and the Di Maggio-Sandler model (Di Maggio and Sandler, 1971). These
39 Cap models allow to reproduce the hardening behaviour in compaction of
40 initially loose powders. In the same approach, many extensions of these
41 models for porous materials were developed (Chtourou et al., 2002; Aubertin
42 and Li, 2004; Khoei and Azami, 2005; Park, 2007). The Drucker-Prager Cap
43 model remains one of the most used due to its ability to reproduce shearing
44 and compaction behaviours. The parameters of this model are simply iden-
45 tified by carrying classical tests. The hardening behaviour is described by a
46 Cap parameter dependent on the volumetric inelastic strain (Doremus et al.,

2001; Wu et al., 2005). In these studies, Young's modulus and Poisson's ratio
defining the elastic part are assumed to be constant. In order to reproduce
a possible nonlinear elastic behaviour, some authors have chosen to identify
elastic and yield surface parameters evolving with the relative density (Kim
et al., 2000; Sinka et al., 2003; Michrafy et al., 2004; Han et al., 2008). The
influence of the temperature on the parameters of a Drucker-Prager Cap
model was rarely taken into account (Piret et al., 2004). The thermal effects
were mainly studied in the geotechnical field.

Models inspired on the Modified Cam-Clay model are often used to repro-
duce the behaviour of soils such as clays (Liu and Carter, 2002; Piccolroaz
et al., 2006). It is an elastoplastic model with a yield surface which can
grow or shrink according to the hardening rule. Triaxial and die compaction
tests are widely used to identify the shearing and hardening behaviours. The
hardening behaviour of the material is written in a specific space in which
only two constant parameters are used to define nonlinear elastic and plastic
parts. Furthermore, this model was extended in order to take into account the
temperature effects (Hueckel and Borsetto, 1990; Hueckel and Baldi, 1990;
Tanaka et al., 1995; Sultan et al., 2002) which mainly modify the size of the
yield surface. In the Modified Cam-Clay model, the size of the yield surface
follows the evolution of the yield stress under hydrostatic compression p_c .
According to the extensions of the Modified Cam-Clay model, this evolution
can be of exponential or polynomial form with various parameters to identify.
For these reasons, the Modified Cam-Clay model was chosen in this work in
order to reproduce the shearing and hardening behaviours of the ramming
mix sensitive to the temperature effect. No tensile strength, nor cohesion are
introduced in this model due to the context of the study mainly focused on
the compacting behaviour.

This paper is organised as follows. Section 2 presents triaxial and die com-
paction tests performed on ramming mix samples with cylindrical shape al-
lowing the investigation of the shearing and hardening behaviours at different
temperatures. A specific calibration step is carried out to know the radial
stress exerted on the sample during the die compaction test. Section 3 de-
scribes the adopted Modified Cam-Clay model. Only one parameter is used
to modify the size of the yield surface in order to reproduce the temperature
effect. An extension of this model to high-compressive pressures is also in-
troduced. The various parameters of this model are identified from triaxial
and die compaction tests data. Finally in section 4, the relevance of the
Modified Cam-Clay model is first confirmed by comparison of the numerical

85 predictions to experimental data obtained from tests used for the identifi-
 86 cation of the model parameters. Finally, a hydrostatic compression test at
 87 room temperature and a die compaction test with transient heating validate
 88 the ability of this model to reproduce the behaviour of the studied ramming
 89 mix.

90 **2. Characterization of the ramming mix behaviour: triaxial and** 91 **die compaction tests**

92 In the high-temperature industry, the ramming mix is used to protect
 93 the steel shell from the expansion of the refractory bricks. Located between
 94 the shell and the bricks, the ramming mix is not directly subjected to the
 95 thermal load applied on the masonry. It is mainly stressed in compression at
 96 low strain rates for a temperature range between 20°C and 80°C. Triaxial and
 97 die compaction tests are carried out to identify the shearing and hardening
 98 behaviours at different temperatures and strain rates. The three-dimensional
 99 stress state is defined by two invariants: the equivalent pressure stress p and
 100 the von Mises equivalent stress q . They are defined as follows:

$$p = -\frac{1}{3}\text{trace}(\underline{\underline{\sigma}}) \quad (1)$$

101

$$q = \sqrt{\frac{3}{2}\underline{\underline{S}} : \underline{\underline{S}}} \quad (2)$$

102 where $\underline{\underline{S}}$ is the deviatoric part of the stress tensor $\underline{\underline{\sigma}}$, given by:

$$\underline{\underline{S}} = \underline{\underline{\sigma}} + p\underline{\underline{I}} \quad (3)$$

103 $\underline{\underline{I}}$ is the second order identity tensor.

104 In the case of a cylindrical sample submitted to compressive axial and radial
 105 stresses ($\sigma_A < 0$ and $\sigma_R < 0$, respectively), the equivalent pressure stress
 106 reads:

$$p = -\frac{\sigma_A + 2\sigma_R}{3} \quad (4)$$

107 and, the von Mises equivalent stress is:

$$q = |\sigma_A - \sigma_R| \quad (5)$$

108 *2.1. Characterization of the shearing behaviour: triaxial tests*

109 Hereafter, we will describe the testing system required to carry out triaxial
110 tests on the ramming mix. The aim is to characterize the shearing behaviour
111 of this material. Figure 1 depicts the triaxial compression apparatus used to
112 perform the triaxial tests. This apparatus is composed of a cell of a 3.5 MPa
113 capacity, a pressure controller, a 25 mm LVDT sensor and a 10 kN load cell.
114 The cell is filled with water in order to apply a controlled radial stress on the
115 sample. This cell is axially free. The axial displacement of the cell which is
116 measured by the LVDT sensor corresponds to the axial displacement of the
117 lower part of the sample. The upper part of the sample is motionless which
118 yields to the axial compression of the sample. The axial force is measured
119 by the load cell. This testing system ensures that cylindrical samples are
120 submitted to axial loads under a constant radial pressure imposed by the
121 water present inside the cell.

122 *2.1.1. Triaxial test procedure*

123 The tested samples are 50 mm in diameter and 95 mm in height. Each
124 specimen is prepared by a manual precompaction of 240 g of carbon ram-
125 ming mix into a die, up to an average void ratio e of 0.42 ± 0.08 where e is
126 given as follows:

$$e = \frac{\rho_r V}{m} - 1 \quad (6)$$

127 ρ_r is the real density of the material, m and V are the mass and volume of
128 the sample, respectively. For this material, a gas pycnometer test would be
129 the most appropriate for the measurement of the real density. Here using
130 the Le Chatelier densimeter apparatus, the measured real density is $\rho_r =$
131 1820 kg/m^3 . This test consists in the immersion of the ramming mix in oil.
132 Water was avoided to allow a better mixture with the coal tar. With this
133 apparatus, it is impossible to apply a pressure which could favor the filling of
134 all voids by the oil. The grain porosity is the most difficult to fill by the oil.
135 Indeed, a mercury porosimetry on the graphite grains shows that there is a
136 grain microporosity with an average void ratio of $0.02 \mu\text{m}$. The equilibrium
137 of the meniscus of the liquid leads to a simple expression used in porosimetry
138 tests relating the pressure P_l exerted on the liquid to fill the voids and the
139 average diameter d of these voids:

$$P_l = \frac{|4\gamma\cos(\alpha)|}{d} \quad (7)$$

140 where γ is the interfacial tension and α is the wetting angle between the
141 liquid and the surface of the sample. Considering oil for liquid in the den-
142 simeter test with $\gamma=0.03$ N/m and $\alpha=30^\circ$, equation (7) shows that a pressure
143 P_l of 5 MPa is required to fill the grain microporosity. Thereby, for the Le
144 Chatelier densimeter test only macroporosities are filled and so e denotes a
145 macro void ratio.

146 In the case of the triaxial test, the initial macro void ratio of the sample is
147 heterogeneous due to a manual compaction mode. This sample is set into an
148 elastomer film to prevent the penetration of water. During the triaxial test,
149 the sample is first submitted to a constant hydrostatic pressure $p = -\sigma_R$.
150 Then, the axial displacement of the cell at constant velocity and radial pres-
151 sure implies the increase of the axial stress on the sample following a stress
152 path defined by the linear relation $q = 3p$ between the stress invariants.

153 *2.1.2. Triaxial test results: temperature and strain rate effects*

154 At room temperature, triaxial tests were carried out for confining pres-
155 sures from 100 kPa to 800 kPa with velocities of 0.1 mm/min, 0.5 mm/min
156 and 1 mm/min. To study the influence of the temperature on the shearing
157 behaviour, a triaxial apparatus operating at high temperatures as used by
158 Olmo et al. (1996) is necessary. The triaxial apparatus of this study has no
159 available heating control, therefore a specific procedure was followed. The
160 sample is first preheated during two hours, at for example 50°C , it is then set
161 on the triaxial apparatus. In a second step, the cell is filled with preheated
162 water at 50°C . In order to minimize the decrease of temperature during the
163 test, a velocity of 1 mm/min was chosen for the triaxial tests at 50°C and
164 80°C . The strain rate effect is so not considered at elevated temperatures.
165 For each triaxial test, a critical shearing stress is reached when the increase
166 of the von Mises equivalent stress stops. As presented in figure 2 for triaxial
167 tests with a confining pressure of 200 kPa, there is no effect of the strain rate
168 at room temperature. Only the temperature influences the critical shearing
169 stress which decreases.

170 *2.2. Characterization of the hardening behaviour: die compaction tests*

171 A hydrostatic compression test is classically used to identify the hardening
172 behaviour of porous materials. An oedometer test on a confined cylindrical
173 sample constitutes also an acceptable solution but requires to be instru-
174 mented in order to measure both axial and radial stresses applied on the
175 sample. The axial stress is easy to get due to a load cell located above the

176 sample. The radial stress is applied by the confinement of a hollow cylinder.
177 In some cases, it is possible to dispose of a load sensor located in the die
178 in order to have a direct measure (Mesbah et al., 1999; Sinka et al., 2003).
179 Otherwise, simple relations can be established between the external circum-
180 ferential strain of the hollow cylinder and the radial stress applied on the
181 sample. The identification of this calibration relation is detailed hereafter.
182 An instrumented die compaction test on a static press INSTRON 5800R was
183 developed as presented in figure 3. Axial displacement and axial load are
184 acquired with a 50 mm LVDT sensor and a 250 kN load cell, respectively.
185 Thanks to a heating control system, compaction tests at elevated tempera-
186 tures are possible. A heating collar with an integrated K-type thermocouple
187 linked to the thermal control is set around the free cylinder. A water-cooling
188 system is added between the load cell and the upper piston in order to avoid
189 the expansion of the load cell during these tests which could affect the mea-
190 surements. Moreover, a double-effect compaction is chosen (free die in the
191 axial direction) to compress equally the sample at the top and the bottom.
192 The die/sample interface is lubricated with a silicon grease to homogenize
193 the radial stresses applied on the height of the sample. The friction coeffi-
194 cient between the final compacted sample and the lubricated die was taken
195 to be 0.22. This value was measured with an inclined plane apparatus. It
196 represents an estimation of the friction coefficient which evolves (decreases
197 globally) when the sample is compacted due to the decrease of the roughness
198 of the lateral area of the ramming mix sample. Finally, 8 circumferential
199 gauges are set around the die in order to evaluate its average circumferen-
200 tial strain. These gauges are located at mid-height of the die with 70 mm
201 between the lowest and the highest ones. They allow to record strains of the
202 die for samples higher than 70 mm.

203 *2.2.1. Calibration test on a rubbery sample*

204 The calibration relation can be identified experimentally from a die com-
205 paction test on an incompressible rubbery sample (Mosbah et al., 1997; Gein-
206 dreau et al., 1999; Hong et al., 2008; Michrafy et al., 2009) or numerically
207 when the circumferential strain of the hollow cylinder is known (Bier et al.,
208 2007). In this study, we choose to carry out a calibration test with an in-
209 compressible sample. It is worth noting that for an incompressible rubbery
210 sample submitted to a confined load, there is an equality between the axial
211 and radial stresses. In this case, it is possible to identify a linear relation
212 between the applied hydrostatic pressure P_h and the average of the circum-

213 differential strains of the die $\varepsilon_{\theta\theta}^{die}$ measured by gauges as follows:

$$C(H_s) = \frac{P_h}{\varepsilon_{\theta\theta}^{die}} \quad (8)$$

214 H_s is the height of the sample. $C(H_s)$ is the function to identify which can
 215 depend on the height of the sample. Figure 4 illustrates the evolution of
 216 $\frac{P_h}{\varepsilon_{\theta\theta}^{die}}$ as a function of the height of the sample. Eight die compaction tests
 217 show a constant value for the C parameter when the contact between the die
 218 and the sample is established. These tests carried out on rubbery samples of
 219 102 mm in height (6 tests) and 92 mm in height (2 tests) allow to identify
 220 the following value for C :

$$C_{test} = 51 \text{ GPa} \quad (9)$$

221 This experimental value can be compared with a theoretical one obtained
 222 for the case of a hollow cylinder submitted to an internal pressure p_1 . This
 223 cylinder has a height L , an internal and an external radius R_1 and R_2 , re-
 224 spectively. The behaviour of the cylinder is assumed to be linear elastic with
 225 a Young's modulus E and a Poisson's ratio ν . For this cylinder, the local
 226 stress field (Salençon, 2007) is given by:

$$\sigma_{rr} = \frac{p_1 R_1^2}{R_2^2 - R_1^2} \left(1 - \left(\frac{R_2}{r} \right)^2 \right) \quad (10)$$

227

$$\sigma_{\theta\theta} = \frac{p_1 R_1^2}{R_2^2 - R_1^2} \left(1 + \left(\frac{R_2}{r} \right)^2 \right) \quad (11)$$

228 where r is the local radius ($R_1 \leq r \leq R_2$). Then, taking into account the
 229 boundary conditions:

$$\sigma_{rr}(r = R_2) = 0 \quad (12)$$

230

$$\sigma_{\theta\theta}(r = R_2) = \frac{2p_1 R_1^2}{R_2^2 - R_1^2} \quad (13)$$

231 and the constitutive local Hooke's law:

$$\varepsilon_{\theta\theta} = \frac{1}{E} \sigma_{\theta\theta} - \frac{\nu}{E} (\sigma_{rr} + \sigma_{zz}) \quad (14)$$

232 it is possible to deduce from equation (14) the expression of $\sigma_{\theta\theta}(r = R_2)$ as
 233 follows:

$$\sigma_{\theta\theta}(r = R_2) = E\varepsilon_{\theta\theta}(r = R_2) + \nu\sigma_{zz}(r = R_2) \quad (15)$$

234 The friction between the sample and the cylinder induces a shear stress at
 235 the sample/cylinder interface and consequently an axial stress on the cylinder
 236 which is not taken into account in the theoretical result. For the carried tests,
 237 the upper and lower sections of the steel cylinder are free and thus (Salençon,
 238 2007):

$$\sigma_{zz}(r = R_2) = 0 \quad (16)$$

239 Equation (15) reads then:

$$\sigma_{\theta\theta}(r = R_2) = E\varepsilon_{\theta\theta}(r = R_2) \quad (17)$$

240 Finally, combining equations (13) and (17), we deduce a theoretical estima-
 241 tion for the C parameter:

$$C_{theory} = \frac{p_1}{\varepsilon_{\theta\theta}(r = R_2)} = \frac{E}{2} \left(\left(\frac{R_2}{R_1} \right)^2 - 1 \right) \quad (18)$$

242 For the considered die: $R_1 = 40.6$ mm, $R_2 = 50$ mm and $E = 210$ GPa.
 243 From equation (18), the theoretical constant is set to:

$$C_{theory} = 54 \text{ GPa} \quad (19)$$

244 The 6% deviation with the experimental result is due to the neglected friction.
 245 The above theoretical study allows to validate the identified experimental
 246 value even if it neglects the friction at the sample/cylinder interface. As a
 247 conclusion, this calibration step provides an estimation for the average radial
 248 stress ($\sigma_{rr} = C_{test} \varepsilon_{\theta\theta}^{die}$) of the ramming mix sample during a die compaction
 249 test.

250 *2.2.2. Die compaction tests at different temperatures and strain rates*

251 For the compaction tests, 700 g of carbon ramming mix are poured into
 252 a die and precompacted with the apparatus up to an initial macro void ratio
 253 of 0.37 ± 0.08 . The precompaction step induces an axial force close to 1 kN
 254 and a radial stress allowing to maintain the mid-height of the free cylinder

255 aligned with the mid-height of the initial sample. The initial sample is 81 mm
256 in diameter and 102 mm in height which gives an aspect ratio higher than
257 1 as mentioned in Doremus et al. (2001) allowing to minimize the stress
258 gradients in the sample. This aspect ratio and the double-effect compaction
259 system allow to assume that the initial macro void ratio is homogeneous.
260 For tests at elevated temperature, strains are recorded during heating and
261 dwell time in order to take the expansion into account. Load/unload cycles
262 are programmed to identify both elastic and plastic parts of the hardening
263 behaviour. Results of these cycles at different temperatures (20°C, 50°C and
264 80°C) and velocities (0.1 mm/min and 1 mm/min) are presented in figure 5.
265 The two curves corresponding to the tests at room temperature at rates
266 of 0.1 mm/min and 1 mm/min are very close. In the same way, the two
267 curves at a temperature of 50°C merge. The strain rate has no effect on the
268 hardening behaviour. The repeatability of the die compaction test is checked
269 at 80°C and 1 mm/min. It is observed that only the temperature influences
270 the hardening behaviour. For the same consolidation state, the axial load
271 decreases with respect to the temperature. This phenomenon is observed
272 in figure 6 where the hardening behaviour with heating is compared with
273 the one at room temperature. For this test carried out under a velocity of
274 0.4 mm/min, the sample has an initial macro void ratio of 0.34 ± 0.08 . During
275 this test, a first heating from 20°C to 50°C and a second one from 50°C to
276 80°C were imposed at 3°C/h on the external part of the steel cylinder. The
277 viscous part of the ramming mix induces a slight softening of the axial stress
278 with the increase of the temperature during a die compaction test.

279 *2.2.3. Die compaction tests at high pressures*

280 Figure 7 presents the results of a die compaction test carried out up to
281 high pressures (40 MPa) at room temperature. The first part of the curve
282 showing the "load-displacement" diagram is similar to the plastic part of
283 the hardening behaviour at room temperature presented in figure 5. In fact,
284 until an axial displacement of 27 mm, the macro void ratio is positive and
285 all macro voids are progressively filled. Afterwards due to pressures higher
286 than 4 MPa, the microporosity of the graphite grains is filled by the coal tar.
287 Considering equation (7) with $\gamma=0.03$ N/m and $\alpha=130^\circ$ which are the pa-
288 rameters for a bituminous, a pressure close to 4 MPa is obtained in order to
289 fill the microporosity of the graphite grains. The macro void ratio is negative
290 because the real density does not account for this microporosity.

291

292 As done for the Modified Cam-Clay model, the hardening behaviour is
 293 written in the $(\ln(p), e)$ plane. In figure 8 are depicted the results of the
 294 die compaction tests carried out at room temperature under low and high
 295 pressures. It allows to illustrate the ability of a compaction law with a sole
 296 elastic slope and two plastic slopes to describe the hardening behaviour of the
 297 ramming mix. The formulation of an extended Modified Cam-Clay model is
 298 presented in the following section.

299 **3. Modelling of the ramming mix**

300 *3.1. Modified Cam-Clay formulation*

301 The Modified Cam-Clay model, which is an extension of the original
 302 model developed by Roscoe and Burland (1968) introducing the critical state
 303 concept, is relevant to reproduce the elastic and plastic parts of the hardening
 304 behaviour of the ramming mix. It is also able to take into account the
 305 temperature effect. The proposed model is based on the Modified Cam-
 306 Clay model implemented in the finite element software ABAQUS/Standard
 307 (Abaqus, 2007).

308 *3.1.1. Yield surface of the model*

309 The Modified Cam-Clay model described in figure 9 is based on a yield
 310 surface with an associated flow rule:

$$F = \frac{1}{\beta^2} \left(\frac{p}{a} - 1 \right)^2 + \left(\frac{q}{Ma} \right)^2 - 1 = 0 \quad (20)$$

311 where M is a constant that defines the slope of the critical state line, a is
 312 the size of the yield surface and β is a constant which can modify the shape
 313 of the cap. In this work, this parameter is used to take into account the
 314 temperature effect on the yield surface of the hardening behaviour. It is
 315 worth noting that for a hydrostatic compression p_c , the yield stress is given
 316 by:

$$p_c(T) = a(1 + \beta(T)) \quad (21)$$

317 The yield surface (equation (20)) is written in terms of two stress invariants:
 318 the equivalent pressure stress p and the von Mises equivalent stress q . In this
 319 section, we introduce some notations. The strain tensor $\underline{\underline{\varepsilon}}$ is decomposed in
 320 two parts as follows:

$$\underline{\underline{\varepsilon}} = \underline{\underline{\varepsilon}}^{el} + \underline{\underline{\varepsilon}}^{pl} \quad (22)$$

321 $\underline{\underline{\varepsilon}}^{el}$ denotes the elastic part of the strain field and $\underline{\underline{\varepsilon}}^{pl}$ represents its plastic
 322 part. Each of these strains can be divided into deviatoric and volumetric
 323 parts. The strain field (equation (22)) reads then:

$$\underline{\underline{\varepsilon}} = (\underline{\underline{\varepsilon}}_{dev}^{el} + \underline{\underline{\varepsilon}}_{dev}^{pl}) - (\varepsilon_{vol}^{el} + \varepsilon_{vol}^{pl})\underline{\underline{I}} \quad (23)$$

324 Moreover, the volumetric part of the strain field ε_{vol} can be expressed as a
 325 function of the macro void ratio e and the initial macro void ratio e_0 :

$$\varepsilon_{vol} = \varepsilon_{vol}^{el} + \varepsilon_{vol}^{pl} = \ln \left(\frac{1+e}{1+e_0} \right) \quad (24)$$

326 The strain field evolves then following a hardening behaviour for high p values
 327 and a shearing behaviour for high q values.

328 3.1.2. Shearing behaviour

329 The critical state line is the key point of the model because it allows to
 330 define hardening and softening behaviours of the material. In fact, when
 331 submitted to an increasing deviatoric stress for a constant value of p lower
 332 than a , the material exhibits a deviatoric elastic behaviour defined by:

$$d\underline{\underline{S}} = 2Gd\underline{\underline{\varepsilon}}_{dev}^{el} \quad (25)$$

333 where G is the shear modulus whose expression is defined by:

$$G = \frac{3(1-2\nu)(1+e_0)}{2(1+\nu)\kappa} p \exp(\varepsilon_{vol}^{el}) \quad (26)$$

334 κ is the logarithmic bulk modulus. Equation (26) demonstrates that G in-
 335 creases with the compaction rate of the material. Then, the yield surface is
 336 reached for values of q upper than the product Mp leading to a softening
 337 behaviour. The yield stress curve decreases and reaches the critical state
 338 line.

339 3.1.3. Hardening behaviour

340 When submitted to hydrostatic pressures, the elastic part of the material
 341 is governed by its volumetric behaviour:

$$\exp(\varepsilon_{vol}^{el}) = 1 + \frac{\kappa}{1+e_0} \ln \frac{p_0}{p} \quad (27)$$

342 where p_0 is the initial value of the equivalent pressure stress. If yielding
 343 occurs, the material exhibits a hardening behaviour described in figure 10
 344 and defined by:

$$de = -\lambda d(\ln p) \quad (28)$$

345 λ is the logarithmic hardening constant for the plasticity. Hereafter, this
 346 slope takes the value of λ_1 for positive macro void ratios and λ_2 for negative
 347 macro void ratios. The hardening behaviour was implemented in the FEA
 348 code ABAQUS thanks to a user defined field (USDFLD) subroutine which
 349 computes the macro void ratio of each element constituting the mesh. Then,
 350 two specific logarithmic hardening constants function of the macro void ratio
 351 are defined.

352 The hardening behaviour is characterized by the growth of the yield surface
 353 size defined by:

$$a = a_0 \exp \left[(1 + e_0) \frac{1 - \exp(\varepsilon_{vol}^{pl})}{\lambda - \kappa \exp(\varepsilon_{vol}^{pl})} \right] \quad (29)$$

354 where a_0 is the initial position of a . This initial overconsolidation is computed
 355 as follows:

$$a_0 = \frac{1}{2} \exp \left(\frac{e_1 - e_0 - \kappa \ln p_0}{\lambda - \kappa} \right) \quad (30)$$

356 e_1 denotes the macro void ratio of the ramming mix for a hydrostatic pressure
 357 of 1 MPa. If the critical state line is reached after the yielding, the material
 358 then distorts without any changes in shear stress or volume.

359 Finally, the use of the Modified Cam-Clay model requires 9 parameters:

- 360 • ν and κ for the elastic behaviour,
- 361 • λ_1 and λ_2 for the plastic behaviour,
- 362 • M for the critical state line,
- 363 • β for the yield surface evolving with the temperature,
- 364 • e_0 , e_1 and p_0 defining the initial state of the material.

365 *3.2. Parameters identification*

366 For different temperatures, the shearing parameter M is identified from
367 triaxial tests described in section 2.1.2. Results of the die compaction tests
368 (section 2.2.2), written in the $(\ln(p), e)$ plane, allow to obtain the parameters
369 of the hardening behaviour. The temperature effect on the parameters of this
370 model is particularly observed.

371 *3.2.1. The critical state line*

372 From the results of the triaxial tests mentioned in section 2.1.2, the critical
373 shearing stresses permit to plot the critical state line. Considering no effect
374 of the velocity, a single value of M was identified at room temperature:
375 $M_{20^\circ C} = 1.18$ as presented in figure 11. Results of tests carried out at $50^\circ C$
376 and $80^\circ C$ are depicted in the same figure. All of them are located under the
377 critical state line identified at room temperature. Since there is no thermal
378 control during these tests, we can only conclude the global influence of the
379 temperature on the slope of the critical state line but nothing on the real
380 value of the parameter M . For this reason, a slight decrease of the slope was
381 assumed for this range of temperatures: $M_{50-80^\circ C} = 1.1$.

382 *3.2.2. Parameters of the hardening behaviour*

383 Parameters identification is done in the $(\ln(p), e)$ plane as previously ex-
384 plained. Results of the carried die compaction tests at different temperatures
385 are exploited as in figure 8. The parameters of the hardening behaviour are
386 reported in table 1. Temperature has no effect on the elastic and plastic
387 slopes. As shown in figure 12, only the parameter e_1 decreases with the in-
388 crease of the temperature. It means that for the same hydrostatic pressure
389 (1 MPa), the sample is more compacted at $80^\circ C$ than at $20^\circ C$. This result is
390 directly related to a phenomenon often observed (Hueckel and Baldi, 1990;
391 Sultan et al., 2002): the decrease of the yield surface with respect to the
392 temperature. As written in equation (30), e_1 is only used to compute the ini-
393 tial consolidation state at the corresponding temperature. In this paper, the
394 temperature effect is reproduced with the parameter β which can modify the
395 shape of the cap part. A unit value is set at room temperature: $\beta(20^\circ C) = 1$.
396 In order to assess $\beta(50^\circ C)$ and $\beta(80^\circ C)$, we consider a hydrostatically com-
397 pacted sample heated from the room temperature up to a temperature T
398 without any volume change. It means that during this heating step the con-
399 solidation state a and the void ratio e remain constant. From equation (21),

400 we can write:

$$\beta(T) = \frac{p_c(T)}{a(T)} - 1 \quad (31)$$

401 At room temperature:

$$\beta(20^\circ C) = \frac{p_c(20^\circ C)}{a(20^\circ C)} - 1 = 1 \quad (32)$$

402 Considering the constant consolidation state, it comes at higher tempera-
403 tures:

$$\beta(T) = \frac{p_c(T)}{a(20^\circ C)} - 1 = 2 \frac{p_c(T)}{p_c(20^\circ C)} - 1 \quad (33)$$

404 According to equation (28) and the parameters e_1 , λ_1 , λ_2 reported in table 1,
405 it is possible to compute the values $p_c(50^\circ C)$ and $p_c(80^\circ C)$ from a chosen
406 value of $p_c(20^\circ C)$ after heating without any volume change. For $T = 50^\circ C$
407 and $T = 80^\circ C$, equation (33) leads to the following values:

$$\beta(50^\circ C) = 0.56 \quad \text{and} \quad \beta(80^\circ C) = 0.21 \quad (34)$$

408 All the parameters needed for the computation of the Modified Cam-Clay
409 model for the ramming mix are summarized in table 2. The Poisson's ratio
410 ν is set equal to 0.25. The obtained results are in agreement with the ten-
411 dencies of the evolution of the Cam-Clay parameters with the temperature
412 as mentioned in Graham et al. (2001). In fact, heating produces variations
413 of the yield surface size leading to a decrease of the elastic zone.

414 4. Numerical results

415 An axisymmetric numerical analysis of triaxial and die compaction tests
416 used for parameters identification is carried out with the finite element code
417 ABAQUS/Standard 6.7. Two additional tests independent from the pre-
418 vious ones are also modelled in order to validate the model. For all these
419 simulations, the ramming mix behaviour is computed with the parameters
420 previously identified.

421 4.1. Modelling of identification tests

422 To simulate triaxial and compaction tests, the ramming mix sample is
423 meshed with four-node axisymmetric continuum elements. Upper and lower
424 pistons are modelled with rigid supports.

425 *4.1.1. Triaxial tests*

426 For the triaxial test, a hard-contact condition in normal behaviour and a
427 friction coefficient of 0.3 (measured with an inclined plane apparatus between
428 the filter paper and the ramming mix) in tangential behaviour are defined
429 between the sample and pistons. Due to the manual compaction mode, an
430 initial heterogeneous macro void ratio is considered for the sample with an
431 average value of 0.42. For all samples, the heterogeneous distribution of
432 the macro void ratio is assumed to be linear with $e = 0.52$ at the bottom
433 of the sample and $e = 0.32$ at its top. In fact, the initial sample is more
434 compacted in its upper part in order to respect the chosen initial height.
435 This distribution was chosen due to its efficiency to reproduce accurately the
436 shearing behaviour under a radial stress of 100 kPa. As shown in figure 13(a),
437 the sample is first hydrostatically stressed on its upper and lateral areas.
438 Then, an axial displacement is imposed on the lower piston. The axial load
439 is read on the upper piston which is locked. This load corresponds to the
440 one measured by the load cell in figure 1. In fact for the simulation, the
441 axial pressure exerted by water is directly applied on the sample and not on
442 the upper piston. When compacted, the sample takes a convex shape (see
443 figure 13(b)) and is mainly stressed in the center and the corners. Numerical
444 and experimental results compare the evolution of the axial load with respect
445 to the axial displacement. They are shown in figure 14 at room temperature
446 and in figure 15 at higher temperatures (50°C and 80°C). A good agreement
447 is reached between tests and simulations for the shearing behaviour.

448 *4.1.2. Die compaction tests*

449 The die compaction test modelling is reported in figure 16(a), the steel die
450 is meshed with four-node axisymmetric continuum elements. Its behaviour is
451 assumed to be isotropic elastic linear with a Young's modulus $E_{die} = 210$ GPa
452 and a Poisson's ratio $\nu_{die} = 0.3$. Contact conditions are defined between the
453 steel parts and the sample: a hard-contact condition in normal behaviour
454 and a friction coefficient of 0.22 in tangential behaviour as explained in sec-
455 tion 2.2. Due to the double-effect precompaction step, a homogeneous macro
456 void ratio of 0.37 describes the initial state of the sample. It is submitted
457 to an axial displacement imposed by the lower piston. The upper piston
458 is locked and provides the axial load applied on the sample. As shown in
459 figure 16(b), the radial stress distribution in the sample is globally homoge-
460 neous. Moreover, the steel die which axially moves up due to the friction, is
461 radially stressed in compression where it is in contact with the sample and in

462 tensile elsewhere. The axial load response to the axial imposed displacement
463 is studied. As shown in figure 17, elastic and plastic parts of the hardening
464 behaviour accurately fit with the proposed model at room temperature. The
465 same agreement between experimental and numerical results is obtained as
466 well at 50°C and 80°C. Figure 18 shows the necessity to allow for a second
467 plastic slope λ_2 to define the hardening behaviour at high pressures. In order
468 to avoid numerical problems, a sweet transition is defined between the two
469 plastic slopes.

470 *4.2. Validation of the model*

471 *4.2.1. Die compaction test with loads/unloads and heating*

472 A die compaction test with load/unload cycles and heating during the
473 test is first used for the validation of the model. A sample with an initial
474 homogeneous macro void ratio of 0.37 is submitted to a load/unload cycle
475 at a velocity of 0.2 mm/min and an increase of the temperature in two
476 steps: first from 20°C to 50°C and then from 50°C to 80°C as shown in
477 figure 19. The thermal field was measured by a thermocouple during the
478 test and applied in the simulation on the external part of the free cylinder.
479 Thanks to a preliminary thermal computation in transient state with the
480 steel and ramming mix thermal properties defined in table 3, the evolution
481 of the temperature in the ramming mix sample is known. Numerical and
482 experimental results for this test are depicted in figure 20. The efficiency of
483 the model to reproduce accurately the hardening behaviour of the material
484 evolving with the temperature is validated.

485 *4.2.2. Hydrostatic compression test*

486 A second test using the triaxial apparatus is developed as well. The idea
487 is to carry out a hydrostatic compression test with loads and unloads, with
488 the only use of the pressure exerted by water. For the ramming mix sam-
489 ple preparation, a similar procedure to that described for triaxial tests was
490 adopted. As shown in figure 21, the cell is axially locked like the upper piston
491 which has no contact with the sample. So no axial displacement is applied
492 on the sample and no axial load is measured by the load cell. The sample is
493 put on the lower locked piston and a cylindrical disk is set above in order to
494 attach the elastomer film. The sample is then hydrostatically stressed on the
495 lateral and upper areas. In order to evaluate the distortion of the sample,
496 the axial displacement of the center of the cylindrical disk above the sample

497 is investigated. The sample being in the cell filled with water, a direct mea-
498 surement is impossible. For this reason a marker tracking method (Nugent
499 et al., 2000; Lee et al., 2009) is used. Markers are drawn on the cylindrical
500 disk. A 8-bit CCD camera allows to grab images of the marked area for each
501 hydrostatic stress increment of 50 kPa. The displacement field of the center
502 of the cylindrical disk can be computed. We assume that this displacement
503 corresponds to the one of the upper part of the sample. Figure 22 shows
504 the experimental and numerical evolutions of the axial displacement of the
505 upper part of the sample with respect to the hydrostatic stress. Unlike the
506 plastic part which is well-reproduced, the elastic part does not seem to be ac-
507 curately reproduced by the model. It can be explained by the loss of contact
508 between the disk and the sample during the unload step. Indeed during the
509 unload, a pump-effect leads to the filling of the space between the cylindrical
510 disk and the sample with air as shown in figure 23. Accordingly, the axial
511 displacement of the cylindrical disk differs from the axial displacement of the
512 upper part of the sample at the end of the unload. During the reload, the
513 air is first evacuated and then the sample is loaded. This phenomenon is
514 not numerically taken into account which leads to slight differences for the
515 elastic part.

516 5. Conclusion

517 In the present paper, a specific ramming mix of the steel industry was
518 studied in order to select an appropriate model reproducing its behaviour.
519 A macroscopic model which is well adapted to engineering applications was
520 retained: the Modified Cam-Clay model which is often used in the geotechni-
521 cal field. It is known for its ability to reproduce the shearing and hardening
522 behaviours. In the proposed model, a single parameter β permits to take
523 into account the temperature effect on the hardening behaviour. Moreover,
524 the hardening behaviour was completed for high pressures defining a second
525 plastic slope. This second slope is related to the microporosity filling. An
526 experimental campaign allowed to determine the material parameters of the
527 proposed model. Triaxial tests allowed to identify the slope of the critical
528 state line of the model and an instrumented die compaction test was con-
529 ceived to characterize the hardening behaviour. For all these tests, no influ-
530 ence of the strain rate was established for strain rates lower than $2 \times 10^{-4} \text{ s}^{-1}$.
531 Only the temperature effect on the critical state line and the yield surface
532 was clearly observed. In fact, the size of the yield surface decreases while

533 the temperature increases. In order to validate the well agreement between
534 experimental and numerical results, two additional tests were carried out.
535 A die compaction test with heating and a hydrostatic compression test at
536 room temperature coupled with a marker tracking method have confirmed
537 the relevance of the model to reproduce the behaviour of the ramming mix.

538 **References**

- 539 Abaqus, 2007. Abaqus Standard Reference Manuals, version 6.7. Simulia,
540 Providence, RI, USA.
- 541 Aubertin, M., Li, L., 2004. A porosity-dependent inelastic criterion for engi-
542 neering materials. *International Journal of Plasticity* 20 (12), 2179–2208.
- 543 Biba, N., Keife, H., Stahlberg, U., 1993. A finite-element simulation of pow-
544 der compaction confirmed by model-material experiments. *Journal of Ma-
545 terials Processing Technology* 36 (2), 141–155.
- 546 Bier, W., Dariel, M., Frage, N., Hartmann, S., Michailov, O., 2007. Die com-
547 paction of copper powder designed for material parameter identification.
548 *International Journal of Mechanical Sciences* 49 (6), 766–777.
- 549 Bousshine, L., Chaaba, A., de Saxcé, G., 2001. Softening in stress-strain
550 curve for Drucker-Prager non-associated plasticity. *International Journal
551 of Plasticity* 17 (1), 21–46.
- 552 Chtourou, H., Guillot, M., Gakwaya, A., 2002. Modeling of the metal pow-
553 der compaction process using the cap model. Part I. Experimental material
554 characterization and validation. *International Journal of Solids and Struc-
555 tures* 39 (4), 1059–1075.
- 556 Di Maggio, F., Sandler, I., 1971. Material model for granular soils. *Journal
557 of the Engineering Mechanics Division* 97 (3), 935–950.
- 558 Doremus, P., Toussaint, F., Alvain, O., 2001. Simple tests and standard pro-
559 cedure for the characterisation of green compacted powder. A. Zavaliangos
560 and A. Laptev (eds.), *Recent Developments in Computer Modelling of
561 Powder Metallurgy Processes*, IOS Press, Amsterdam, 29–41.
- 562 Drucker, D. C., Prager, W., 1952. Soil mechanics and plastic analysis on
563 limit design. *Quarterly of Applied Mathematics* 10(2), 157–165.
- 564 Fleck, N. A., Kuhn, L. T., McMeeking, R. M., 1992. Yielding of metal powder
565 bonded by isolated contacts. *Journal of the Mechanics and Physics of Solids*
566 40 (5), 1139–1162.
- 567 Fleck, N. A., 1995. On the cold compaction of powders. *Journal of the Me-
568 chanics and Physics of Solids* 43 (9), 1409–1431.

- 569 Geindreau, C., Bouvard, D., Doremus, P., 1999. Constitutive behaviour of
570 metal powder during hot forming. Part I: Experimental investigation with
571 lead powder as a simulation material. *European Journal of Mechanics -*
572 *A/Solids* 18, 581–596.
- 573 Graham, J., Tanaka, N., Crilly, T., Alfaro, M., 2001. Modified Cam-Clay
574 modelling of temperature effects in clays. *Canadian geotechnical journal*
575 38, 608–621.
- 576 Gurson, A. L., 1977. Continuum theory of ductile rupture by void nucleation
577 and growth, I. Yield criteria and flow rules for porous ductile media. *Jour-*
578 *nal of Engineering Materials and Technology-Transactions of the ASME*
579 99 (1), 2–15.
- 580 Haggblad, H. A., 1991. Constitutive models for powder materials. *Powder*
581 *Technology* 67 (2), 127–137.
- 582 Han, L., Elliott, J., Bentham, A., Mills, A., Amidon, G., Hancock, B., 2008.
583 A modified Drucker-Prager Cap model for die compaction simulation of
584 pharmaceutical powders. *International Journal of Solids and Structures*
585 45 (10), 3088–3106.
- 586 Helle, A., Easterling, K., Ashby, M., 1985. Hot-isostatic pressing diagrams:
587 New developments. *Acta Metallurgica* 33, 2163–2174.
- 588 Hong, S.-T., Hovanski, Y., Lavender, C. A., Weil, K. S., 2008. Investigation
589 of die stress profiles during powder compaction using instrumented die.
590 *Journal of Materials Engineering and Performance* 17 (3), 382–386.
- 591 Hueckel, T., Baldi, G., 1990. Thermoplasticity of saturated clays: Experi-
592 mental constitutive study. *Journal of Geotechnical Engineering* 116 (12),
593 1778–1796.
- 594 Hueckel, T., Borsetto, M., 1990. Thermoplasticity of saturated soils and
595 shales: Constitutive equations. *Journal of Geotechnical Engineering*
596 116 (12), 1765–1777.
- 597 Khoei, A., Azami, A., 2005. A single cone-cap plasticity with an isotropic
598 hardening rule for powder materials. *International Journal of Mechanical*
599 *Sciences* 47 (1), 94–109.

- 600 Kim, K. T., Choi, S. W., Park, H., 2000. Densification behavior of ceramic
601 powder under cold compaction. *Journal of engineering materials and tech-*
602 *nology* 122, 238–244.
- 603 Le, T. H., Dormieux, L., Jeannin, L., Burlion, N., Barthélémy, J.-F., 2008.
604 Nonlinear behavior of matrix-inclusion composites under high confining
605 pressure: application to concrete and mortar. *Comptes Rendus Mécanique*
606 336, 670–676.
- 607 Lee, J. W., Kim, H. W., Ku, H. C., Yoo, W. S., 2009. Comparison of external
608 damping models in a large deformation problem. *Journal of Sound and*
609 *Vibration* 325, 722–741.
- 610 Liu, M., Carter, J., 2002. A structured Cam Clay model. *Canadian Geotech-*
611 *nical Journal* 39, 1313–1332.
- 612 Mesbah, A., Morel, J. C., Olivier, M., 1999. Comportement des sols fins
613 argileux pendant un essai de compactage statique : détermination des
614 paramètres pertinents. *Materials and Structures/Matériaux et Construc-*
615 *tions* 32, 687–694.
- 616 Michrafy, A., Dodds, J., Kadiri, M., 2004. Wall friction in the compaction of
617 pharmaceutical powders: measurement and effect on the density distribu-
618 tion. *Powder Technology* 148 (1), 53–55.
- 619 Michrafy, A., Diarra, H., Dodds, J., 2009. Compaction behavior of binary
620 mixtures. *Powder Technology* 190 (1-2), 146–151.
- 621 Mosbah, P., Bouvard, D., Ouedraogo, E., Stutz, P., 1997. Experimental tech-
622 niques for analysis of die pressing and ejection of metal powder. *Powder*
623 *Technology* 40, 269–277.
- 624 Nugent, E. E., Calhoun, R. B., Mortensen, A., 2000. Experimental investi-
625 gation of stress and strain fields in a ductile matrix surrounding an elastic
626 inclusion. *Acta Materialia* 48 (7), 1451–1467.
- 627 Olmo, C. D., Fioravante, V., Gera, F., Hueckel, T., Mayor, J., Pellegrini,
628 R., 1996. Thermomechanical properties of deep argillaceous formations.
629 *Engineering Geology* 41 (1-4), 87–102.

- 630 Park, S.-J., Han, H. N., Oh, K. H., Lee, D. N., 1999. Model for compaction
631 of metal powders. *International Journal of Mechanical Sciences* 41 (2),
632 121–141.
- 633 Park, J., 2007. A yield function for copper powder in compaction. *Journal of*
634 *Materials Processing Technology* 187-188, 672–675.
- 635 Piat, R., Reznik, B., Schnack, E., Gerthsen, D., 2004. Modeling of effective
636 material properties of pyrolytic carbon with different texture degrees by
637 homogenization method. *Composites Science and Technology* 64 (13-14),
638 2015–2020.
- 639 Piccolroaz, A., Bigoni, D., Gajo, A., 2006. An elastoplastic framework for
640 granular materials becoming cohesive through mechanical densification.
641 Part I - small strain formulation. *European Journal of Mechanics - A/Solids*
642 25 (2), 334–357.
- 643 Piret, J., Menéndez Arias, J., Franken, M., Blumenfeld, P., 2004. Study
644 of behaviour of cement and mass joint utilised in aggregates of steel
645 industry. *European Commission/Technical steel research - EUR21133 EN*
- 646 Roscoe, K., Burland, J., 1968. On the generalized stress-strain behaviour of
647 wet clay. *Engineering Plasticity*, Heyman J., Leckie F.A. (eds.), Cambridge
648 University Press, 535–609.
- 649 Salençon, J., 2007. *Mécanique des milieux continus. Tome II. Éditions de*
650 *l'École Polytechnique, Palaiseau, Ellipses Paris.*
- 651 Shima, S., Oyane, M., 1976. Plasticity theory for porous metals. *International*
652 *Journal of Mechanical Sciences* 18 (6), 285–291.
- 653 Sinka, I. C., Cunningham, J. C., Zavaliangos, A., 2003. The effect of wall
654 friction in the compaction of pharmaceutical tablets with curved faces: a
655 validation study of the Drucker-Prager Cap model. *Powder Technology*
656 133 (1-3), 33–43.
- 657 Sultan, N., Delage, P., Cui, Y. J., 2002. Temperature effects on the volume
658 change behaviour of boom clay. *Engineering Geology* 64 (2-3), 135–145.
- 659 Tanaka, N., Graham, J., Lingnau, B.E., 1995. A thermal elastic plastic model
660 based on Modified Cam Clay. *10th PanAmerican Conference on Soil Me-*
661 *chanics and Foundations Engineering, Guadalajara, Mexico.*

662 Wu, C.-Y., Ruddy, O., Bentham, A., Hancock, B., Best, S., Elliott, J., 2005.
663 Modelling the mechanical behaviour of pharmaceutical powders during
664 compaction. *Powder Technology* 152 (1-3), 107–117.

665 **List of Figures**

666	1	Triaxial compression test.	26
667	2	Triaxial tests with a confining pressure of 200 kPa at different	
668		temperatures and velocities.	27
669	3	Instrumented die compaction test.	28
670	4	Identification of the calibration relation.	29
671	5	Results of die compaction tests at different velocities and tem-	
672		peratures.	30
673	6	Temperature effect on the hardening behaviour.	31
674	7	Die compaction test under high pressures.	32
675	8	Hardening behaviour in the $(\ln(p), e)$ plane.	33
676	9	Yield surface and critical state line of the Modified Cam-Clay	
677		model.	34
678	10	Compaction behaviour of the Modified Cam-Clay model.	35
679	11	Results of triaxial tests at 3 different temperatures.	36
680	12	Influence of the temperature on the hardening behaviour.	37
681	13	Simulation of the triaxial test: (a) Mesh and boundary condi-	
682		tions, (b) Axial stress distribution.	38
683	14	Triaxial tests with different radial stresses at $T=20^{\circ}\text{C}$	39
684	15	Triaxial tests at $T=50^{\circ}\text{C}$ and $T=80^{\circ}\text{C}$	40
685	16	Simulation of the die compaction test: (a) Mesh and boundary	
686		conditions, (b) Radial stress distribution.	41
687	17	Die compaction test at $T=20^{\circ}\text{C}$	42
688	18	Experimental and numerical results for high pressures.	43
689	19	Temperature evolution during the die compaction test.	44
690	20	Die compaction test with loads/unloads and heating.	45
691	21	Hydrostatic compression test.	46
692	22	Hydrostatic compression test with loads/unloads.	47
693	23	Air pump-effect during the unload for different pressures: (a)	
694		400 kPa, (b) 300 kPa, (c) 150 kPa, (d) 100 kPa.	48

695 **List of Tables**

696	1	Hardening behaviour parameters for the ramming mix.	49
697	2	Modified Cam-Clay model parameters for the ramming mix.	50
698	3	Thermal properties for the steel and the ramming mix.	51

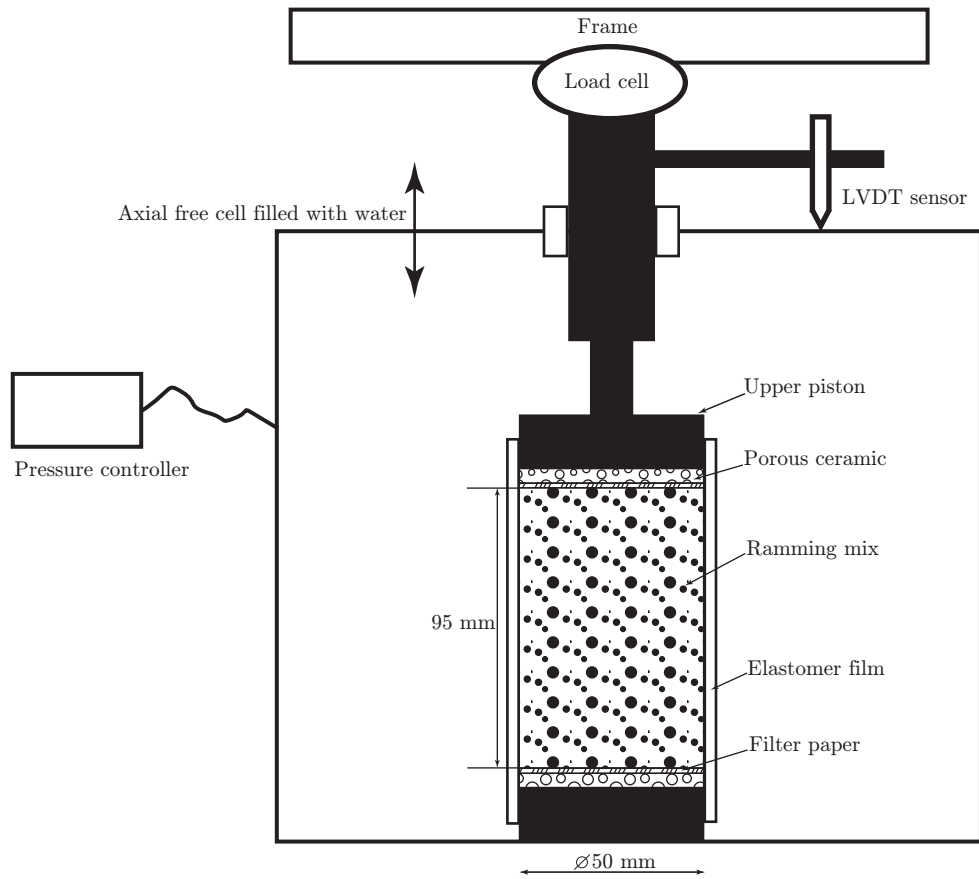


Figure 1: Triaxial compression test.

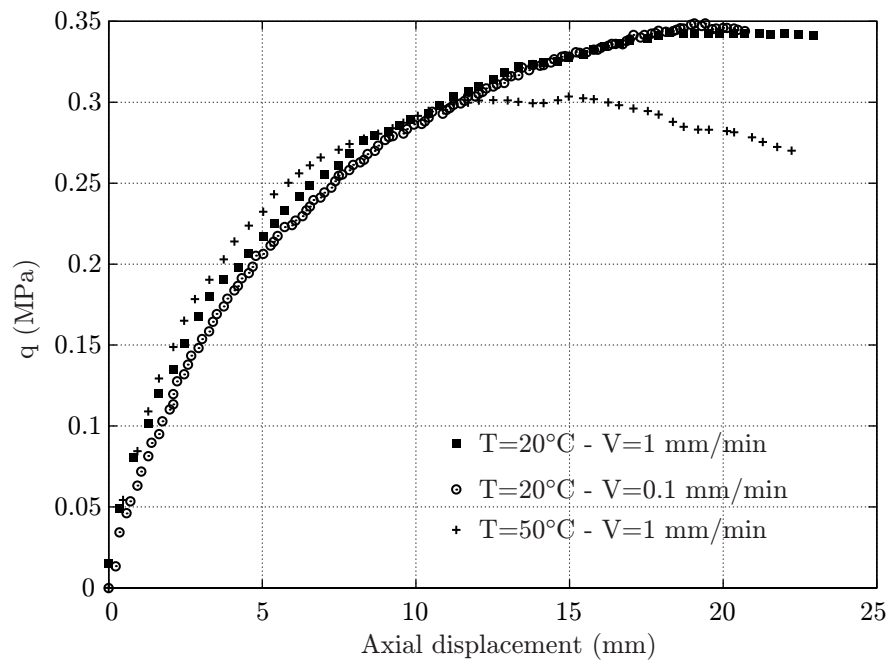


Figure 2: Triaxial tests with a confining pressure of 200 kPa at different temperatures and velocities.

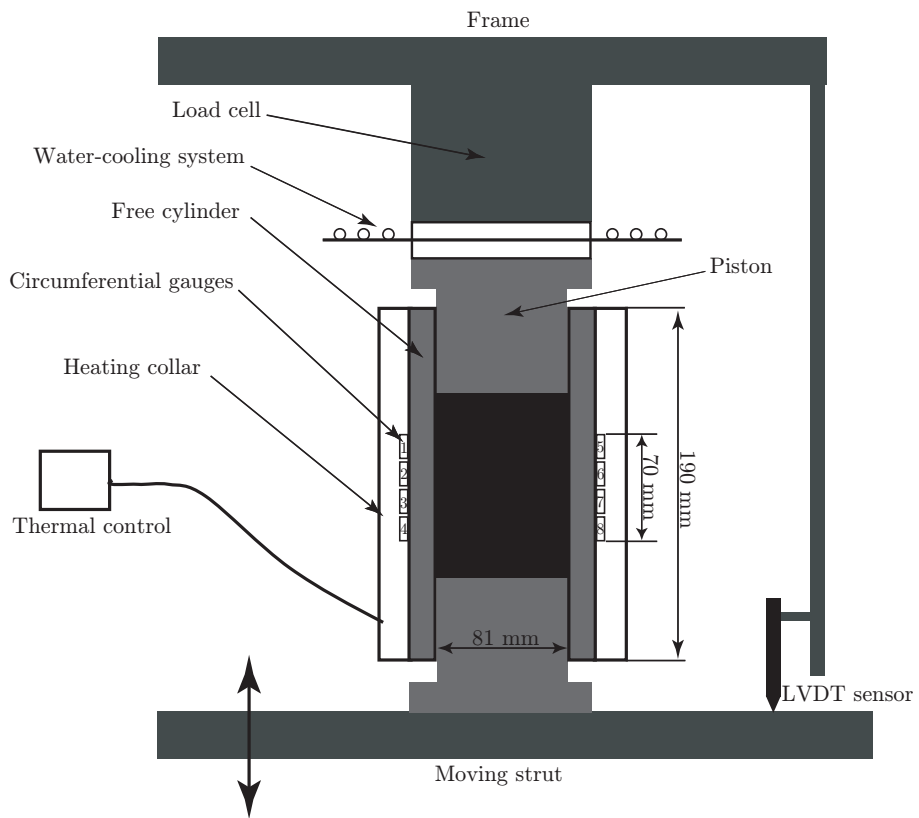


Figure 3: Instrumented die compaction test.

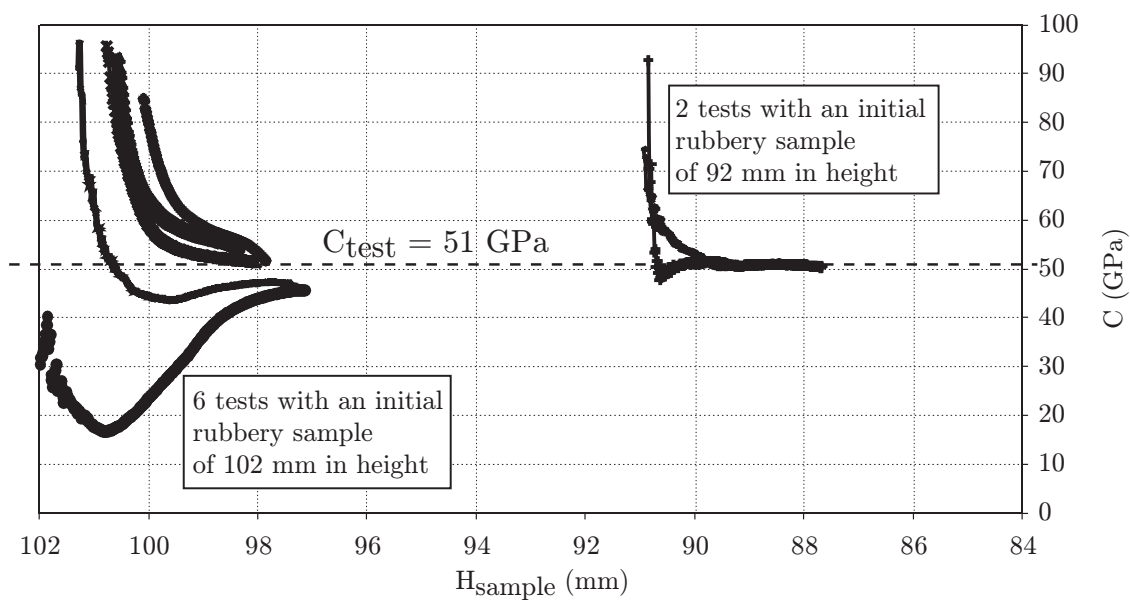


Figure 4: Identification of the calibration relation.

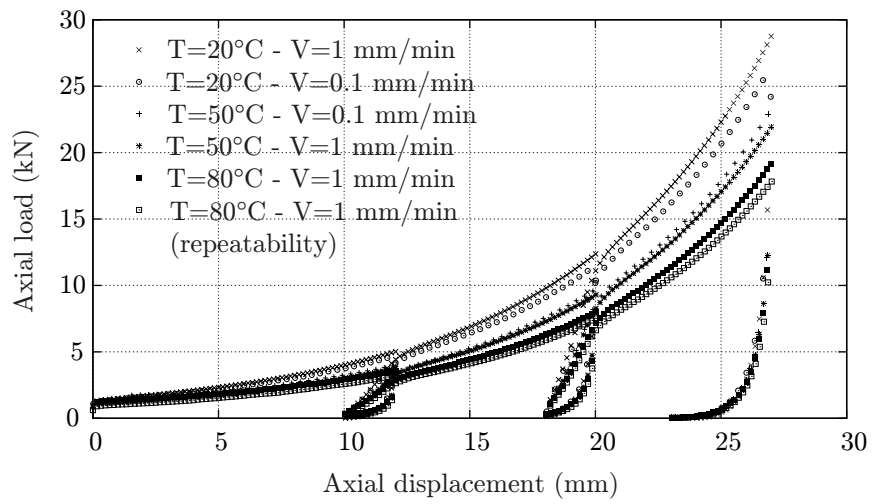


Figure 5: Results of die compaction tests at different velocities and temperatures.

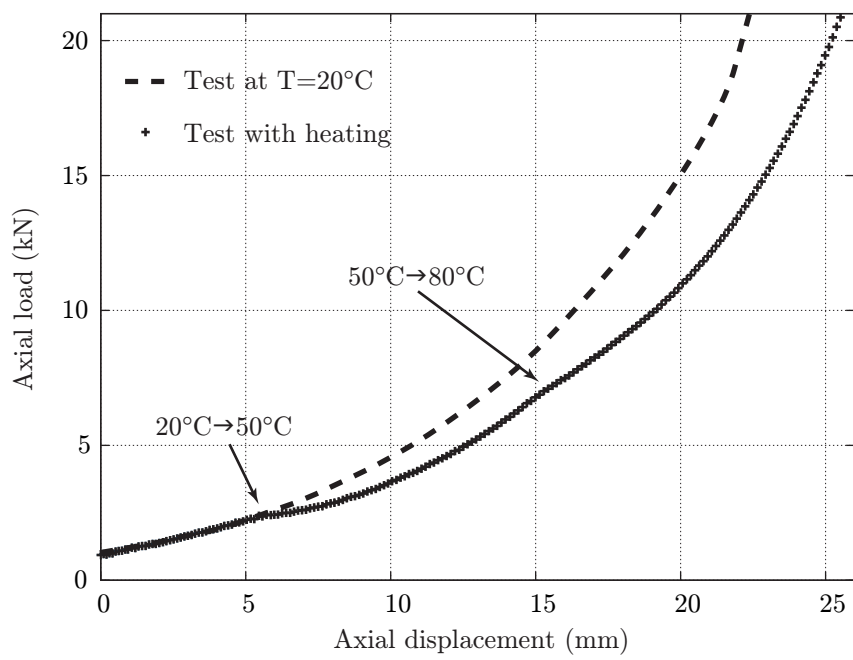


Figure 6: Temperature effect on the hardening behaviour.

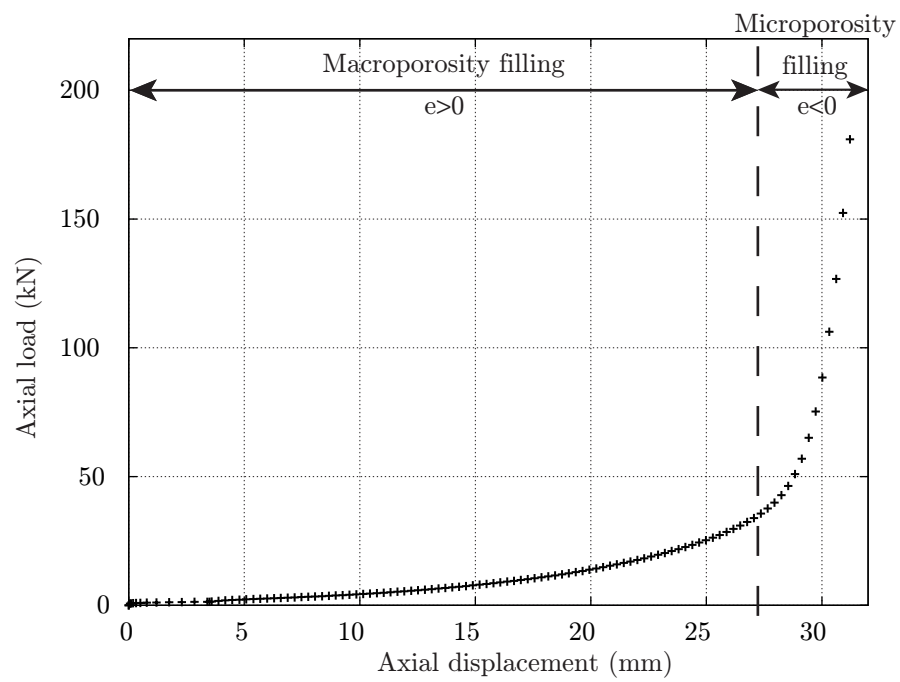


Figure 7: Die compaction test under high pressures.

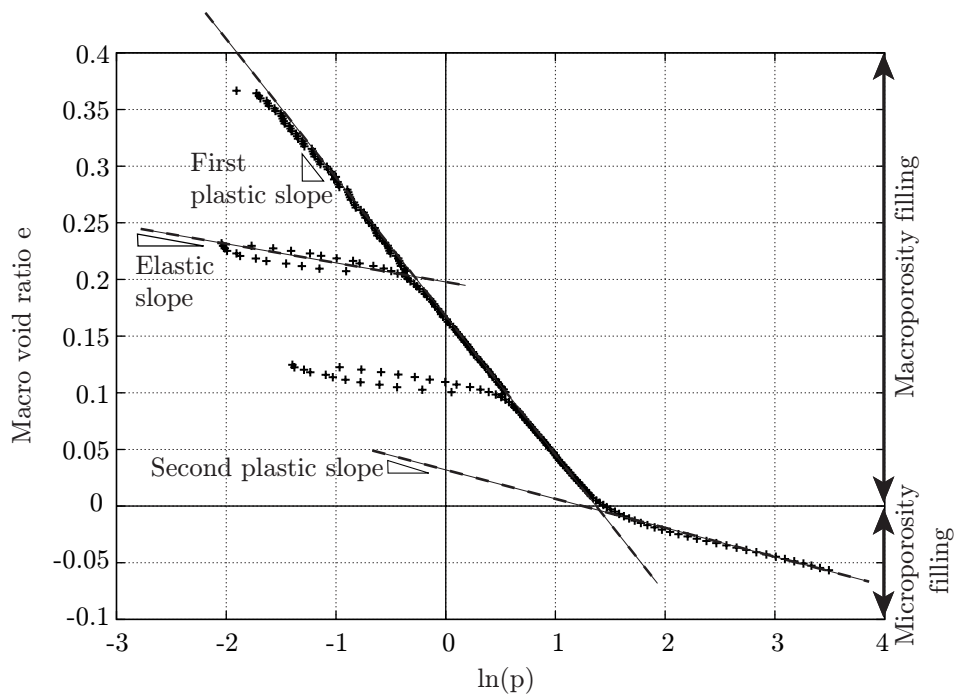


Figure 8: Hardening behaviour in the $(\ln(p), e)$ plane.

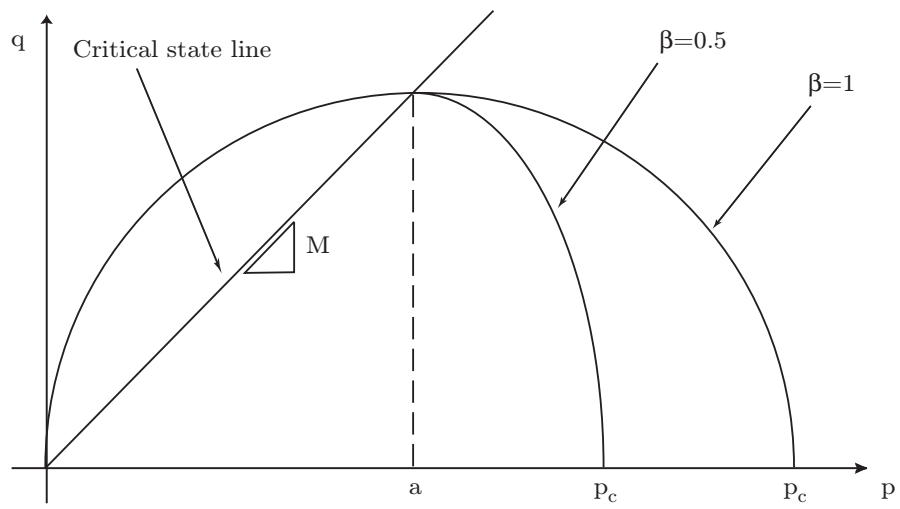


Figure 9: Yield surface and critical state line of the Modified Cam-Clay model.

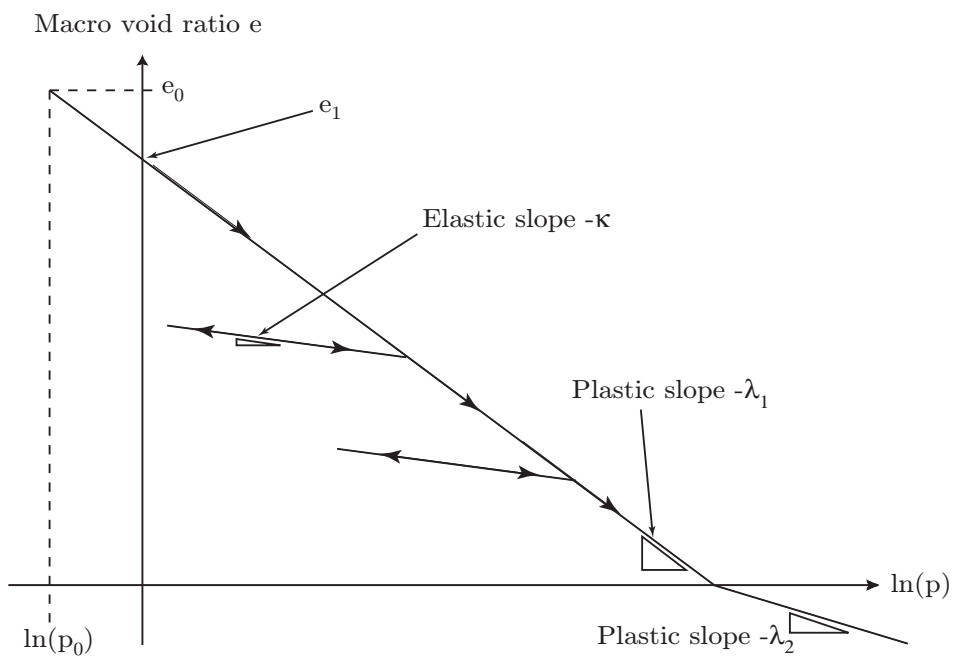


Figure 10: Compaction behaviour of the Modified Cam-Clay model.

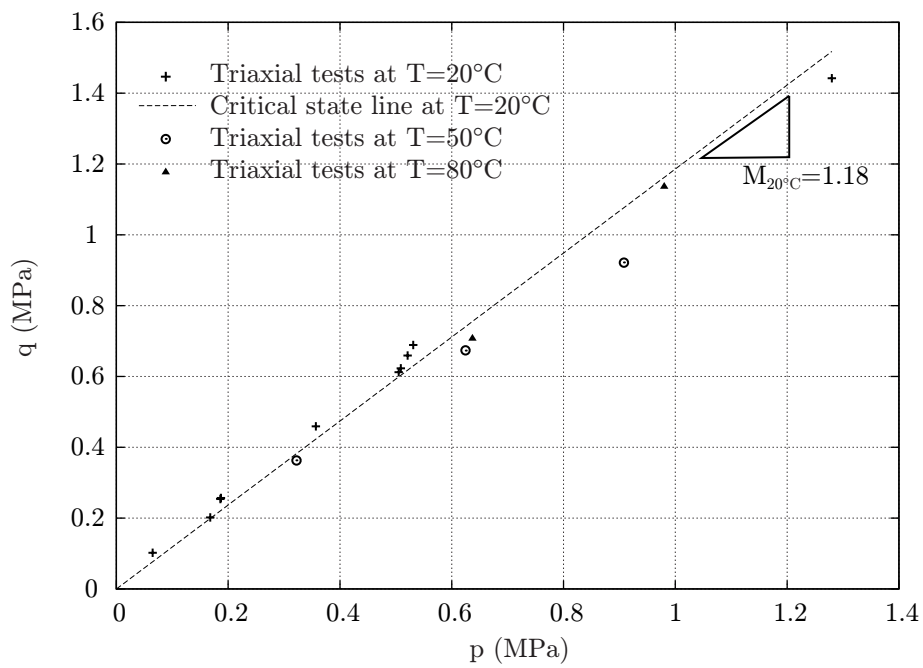


Figure 11: Results of triaxial tests at 3 different temperatures.

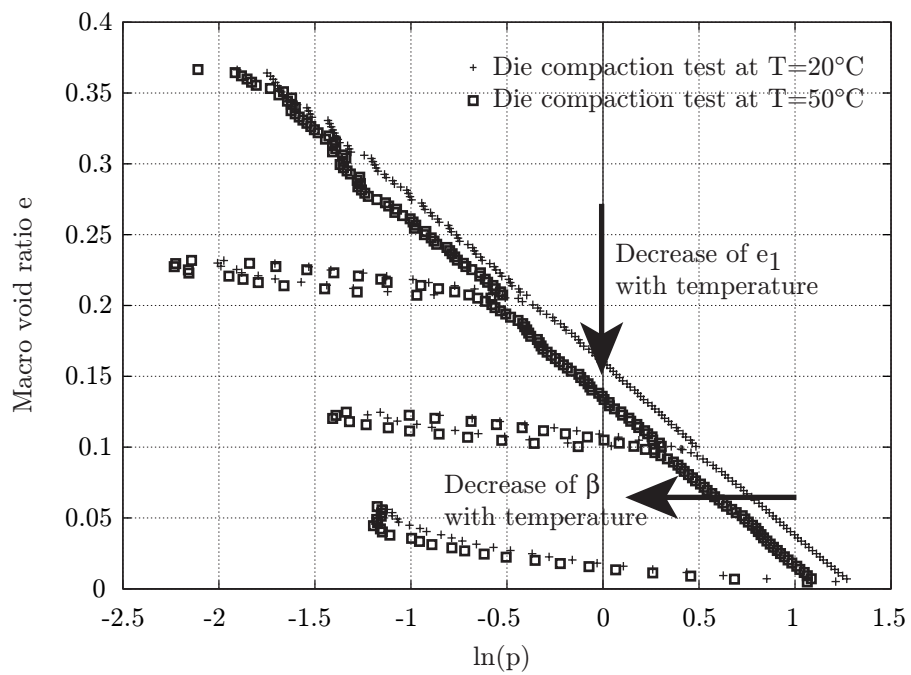


Figure 12: Influence of the temperature on the hardening behaviour.

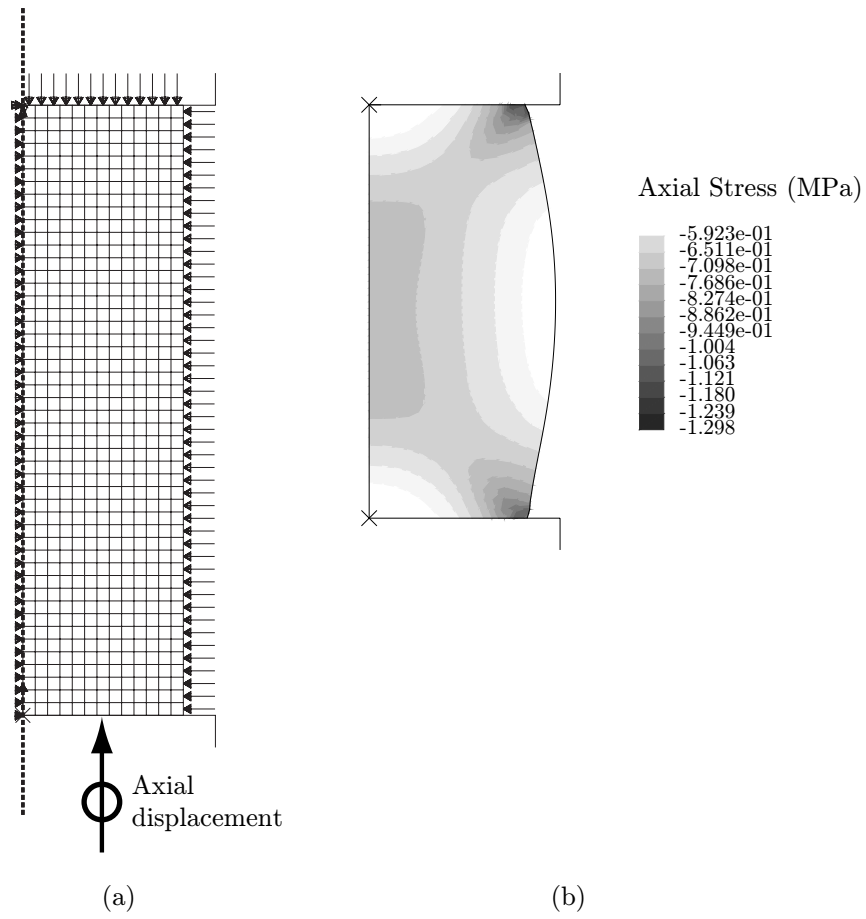


Figure 13: Simulation of the triaxial test: (a) Mesh and boundary conditions, (b) Axial stress distribution.

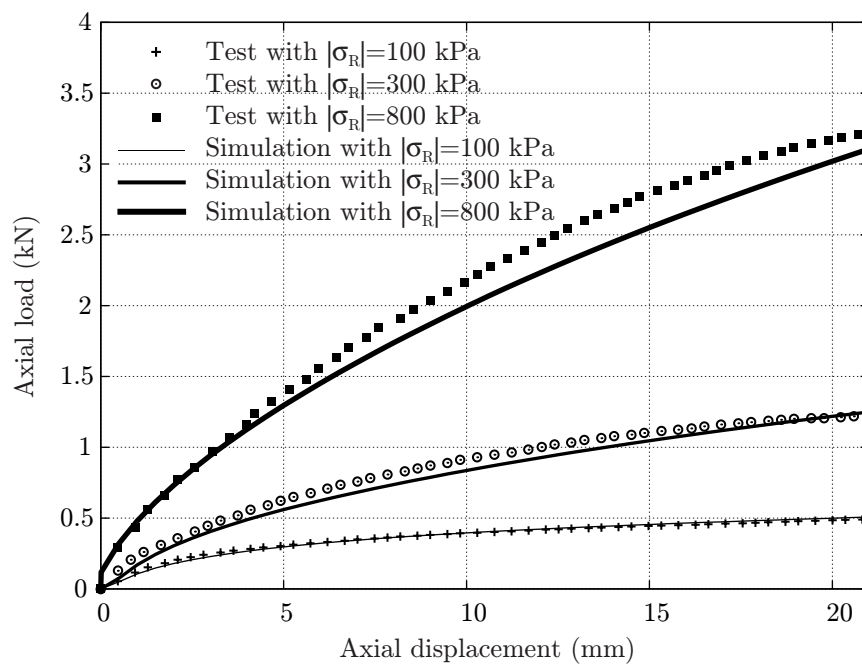


Figure 14: Triaxial tests with different radial stresses at $T=20^\circ\text{C}$.

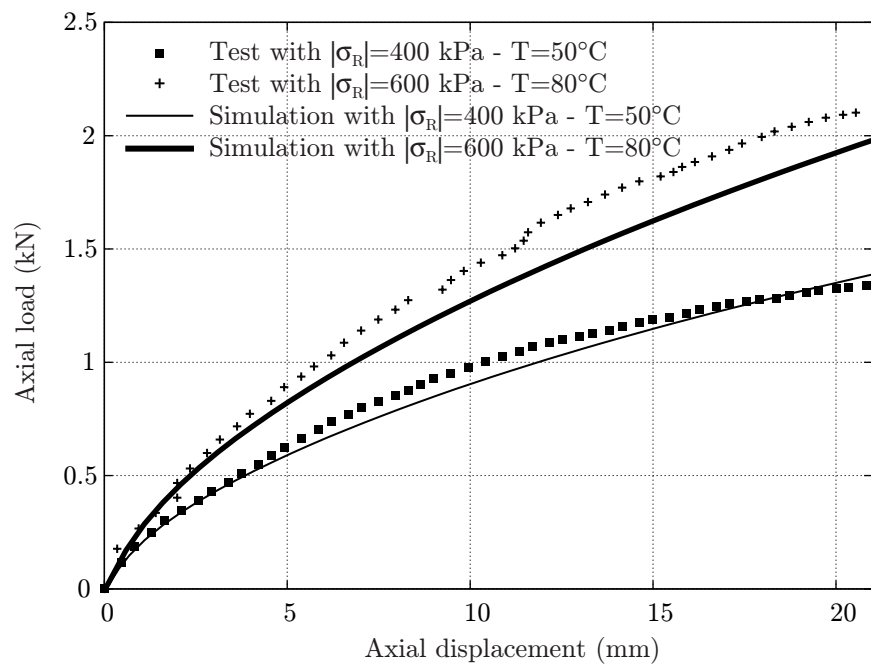


Figure 15: Triaxial tests at T=50°C and T=80°C.

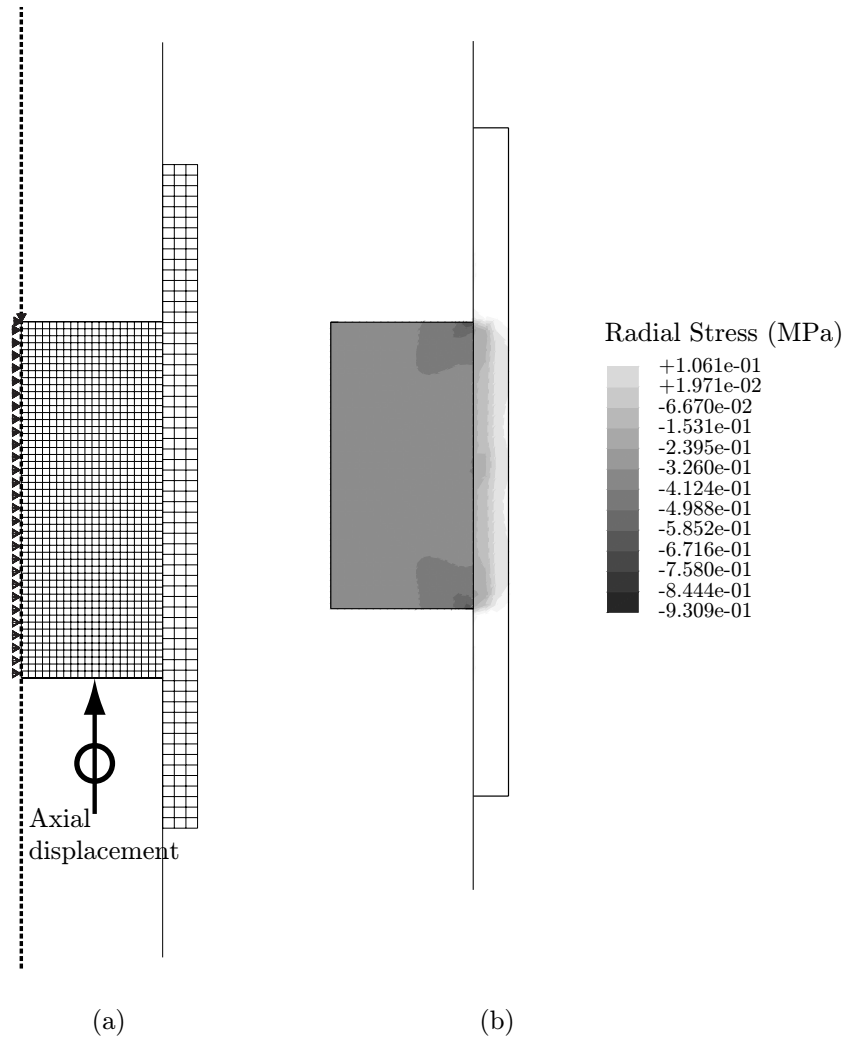


Figure 16: Simulation of the die compaction test: (a) Mesh and boundary conditions, (b) Radial stress distribution.

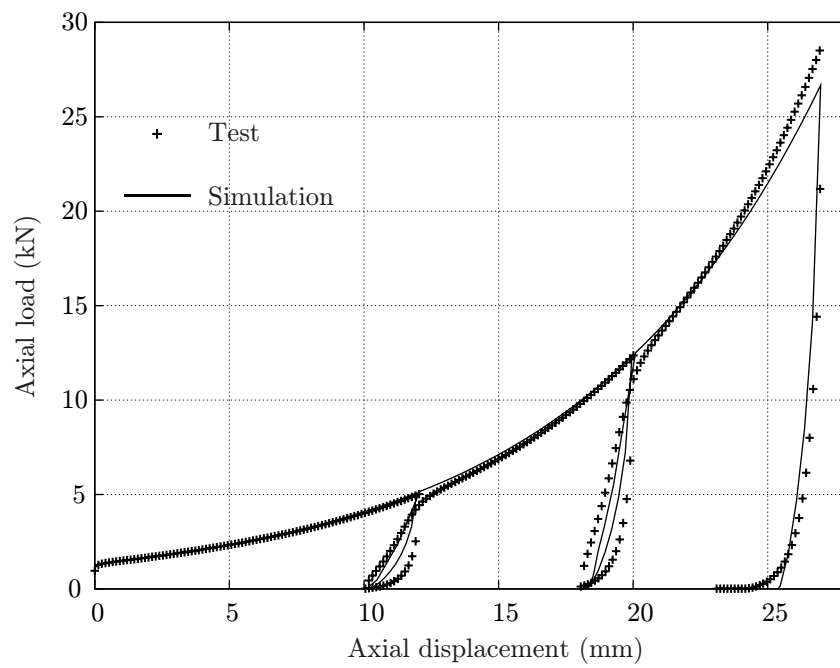


Figure 17: Die compaction test at $T=20^{\circ}\text{C}$.

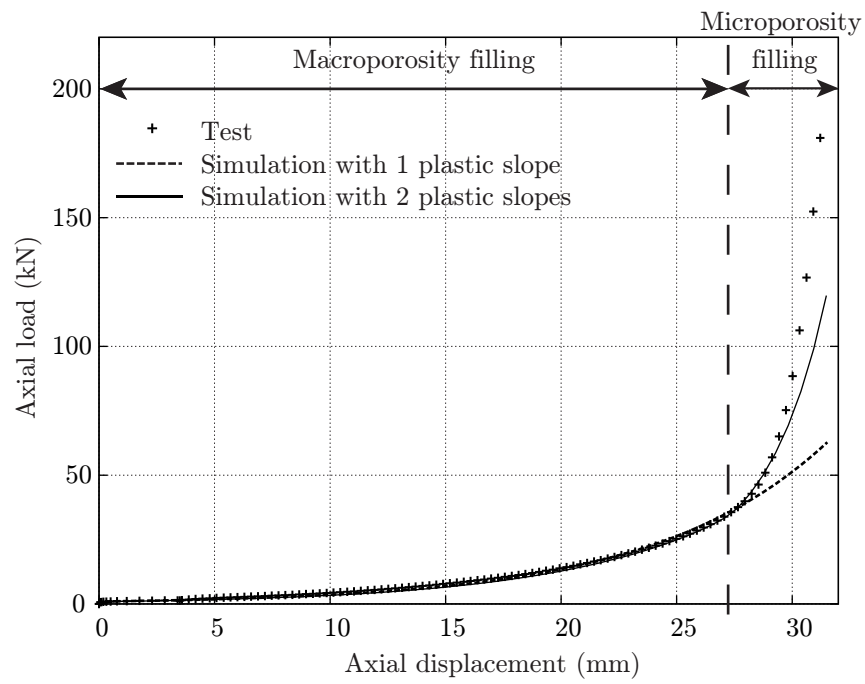


Figure 18: Experimental and numerical results for high pressures.

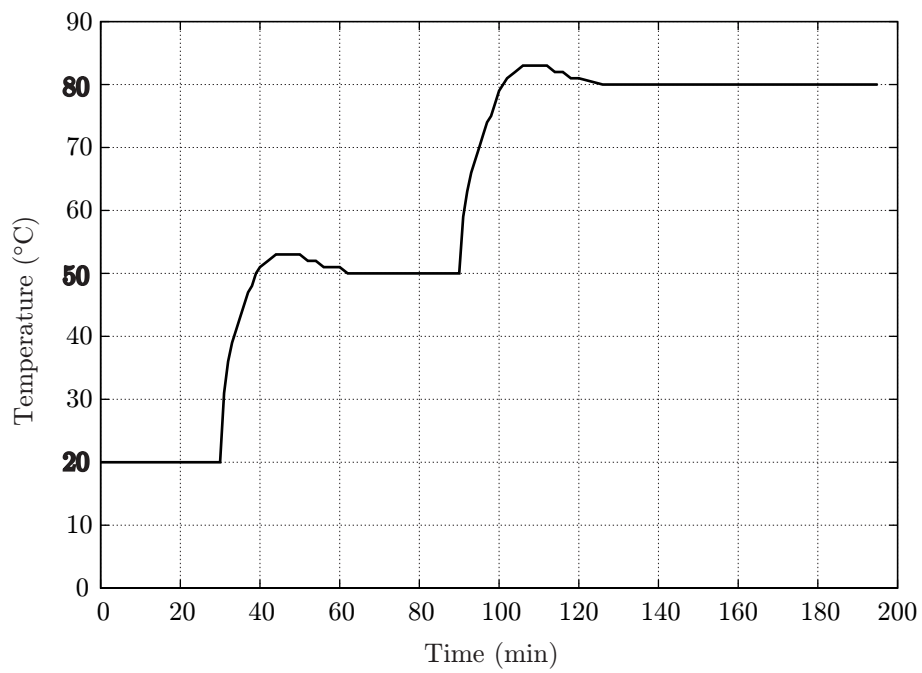


Figure 19: Temperature evolution during the die compaction test.

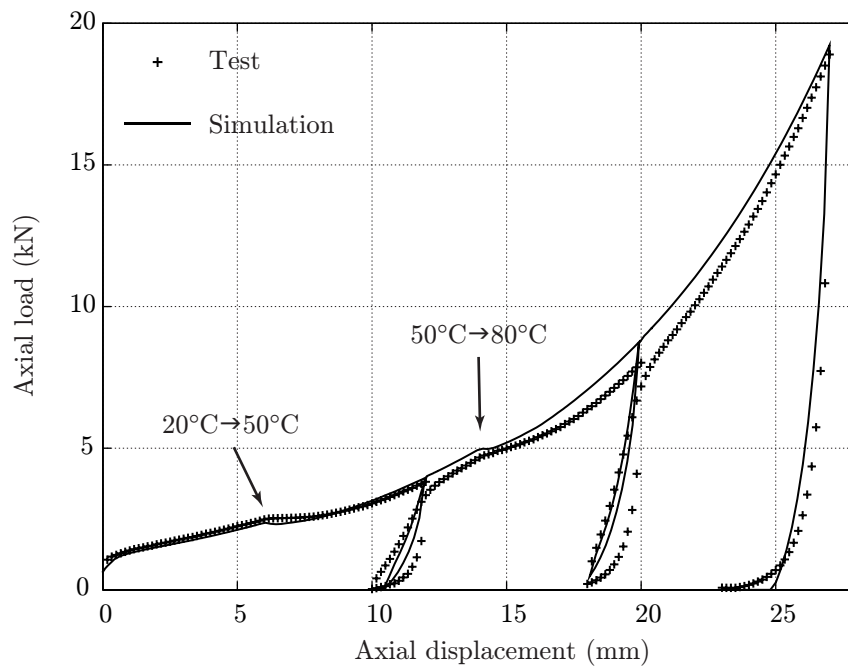


Figure 20: Die compaction test with loads/unloads and heating.

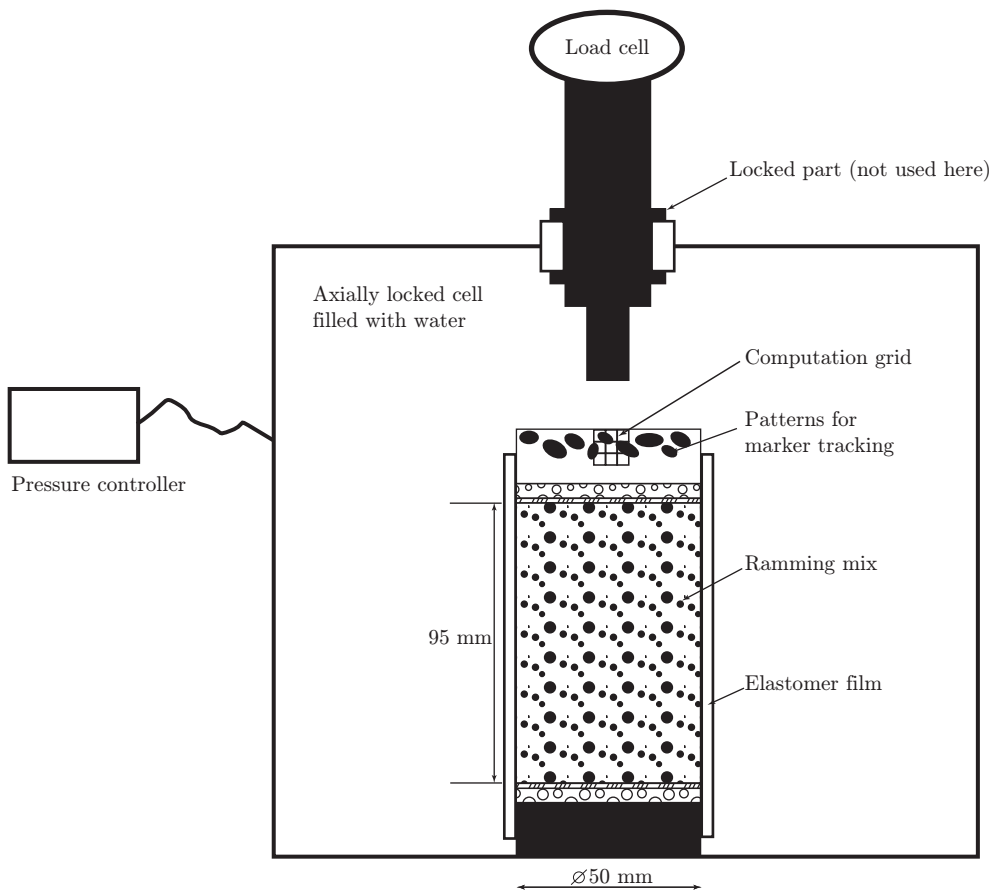


Figure 21: Hydrostatic compression test.

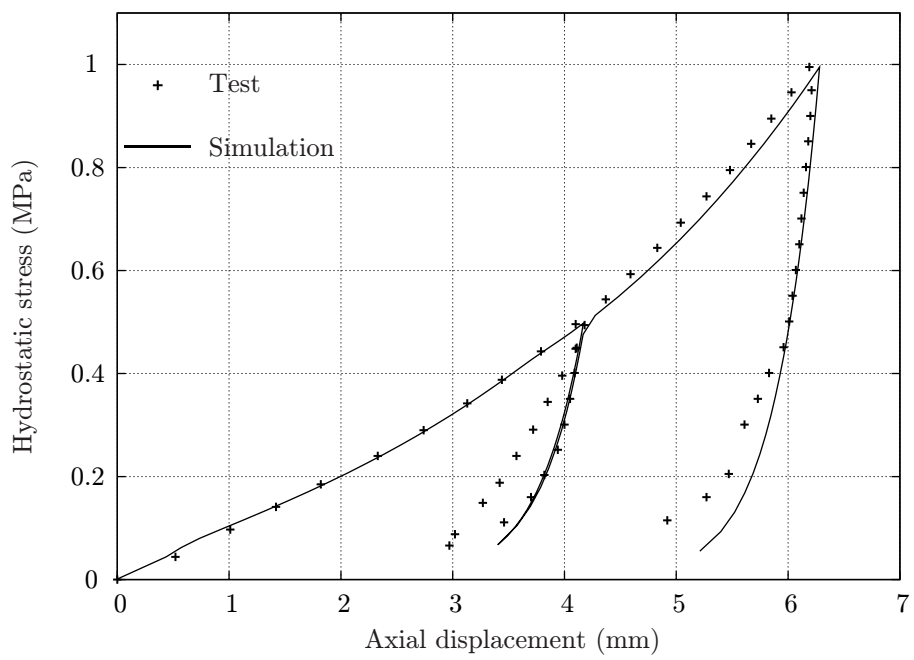
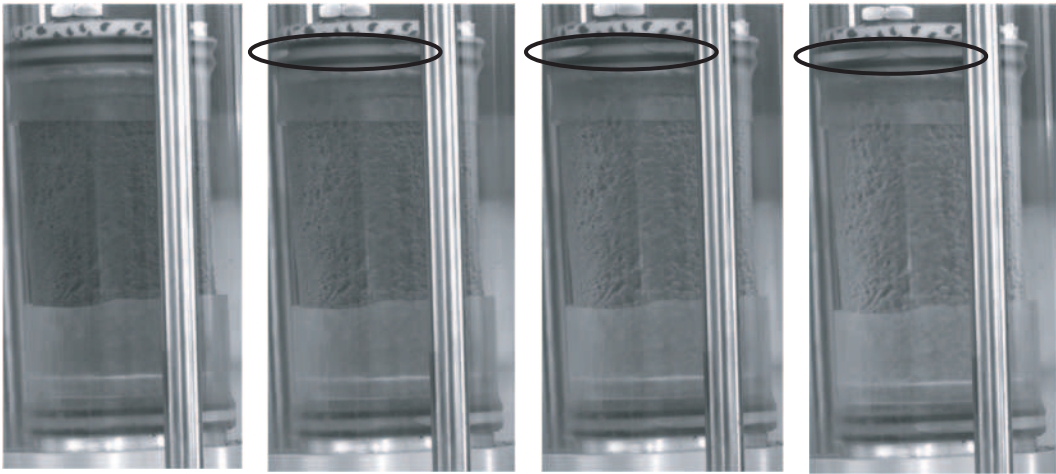


Figure 22: Hydrostatic compression test with loads/unloads.



(a)

(b)

(c)

(d)

Figure 23: Air pump-effect during the unload for different pressures: (a) 400 kPa, (b) 300 kPa, (c) 150 kPa, (d) 100 kPa.

Table 1: Hardening behaviour parameters for the ramming mix.

Temperature (°C)	20	50	80
κ	0.017	0.017	0.017
λ_1	0.12	0.12	0.12
λ_2	0.024	0.024	0.024
e_1	0.16	0.13	0.1

Table 2: Modified Cam-Clay model parameters for the ramming mix.

Temperature (°C)	20	50	80
ν		0.25	
κ		0.017	
M	1.18	1.1	1.1
λ_1		0.12	
λ_2		0.024	
e_1	0.16	0.13	0.1
β	1	0.56	0.21

Table 3: Thermal properties for the steel and the ramming mix.

	Steel	Ramming mix
Density ($\text{kg}\cdot\text{mm}^{-3}$)	7.85×10^{-6}	$[1.33 \times 10^{-6}; 1.73 \times 10^{-6}]$
Conductivity ($\text{W}\cdot\text{mm}^{-1}\cdot\text{K}^{-1}$)	0.047	0.025
Specific heat ($\text{J}\cdot\text{kg}^{-1}\cdot\text{K}^{-1}$)	450	700
Expansion (K^{-1})	1.2×10^{-5}	3.3×10^{-6}